The Astrophysical Journal Letters, 965:L25 (8pp), 2024 April 20 https://doi.org/10.3847/2041-8213/ad3946

Tidal Disruption Encores

Taeho Ryu[1,2], Rosalba Perna[3,4], and Matteo Cantiello[4]
[1] The Max Planck Institute for Astrophysics, Karl-Schwarzschild-Str. 1, Garching, 85748, Germany; tryu@mpa-garching.mpg.de
[2] Physics and Astronomy Department, Johns Hopkins University, Baltimore, MD 21218, USA
[3] Department of Physics and Astronomy, Stony Brook University, Stony Brook, NY 11794-3800, USA
[4] Center for Computational Astrophysics, Flatiron Institute, New York, NY 10010, USA
Received 2024 March 14; revised 2024 March 27; accepted 2024 March 27; published 2024 April 16

Abstract

Nuclear star clusters (NSCs), made up of a dense concentration of stars and the compact objects they leave behind, are ubiquitous in the central regions of galaxies surrounding the central supermassive black hole (SMBH). Close interactions between stars and stellar-mass black holes (sBHs) lead to tidal disruption events (TDEs). We uncover an interesting new phenomenon: for a subset of these, the unbound debris (to the sBH) remains bound to the SMBH, accreting at a later time, thus giving rise to a second flare. We compute the rate of such events and find them ranging within 10^{-6}–$10^{-3}\,\mathrm{yr}^{-1}\,\mathrm{gal}^{-1}$ for SMBH mass $\simeq 10^{6}$–$10^{9}\,M_{\odot}$. Time delays between the two flares spread over a wide range, from less than a year to hundreds of years. The temporal evolution of the light curves of the second flare can vary between the standard $t^{-5/3}$ power law to much steeper decays, providing a natural explanation for observed light curves in tension with the classical TDE model. Our predictions have implications for learning about NSC properties and calibrating its sBH population. Some double flares may be electromagnetic counterparts to LISA extreme-mass-ratio inspiral sources. Another important implication is the possible existence of TDE-like events in very massive SMBHs, where TDEs are not expected. Such flares can affect spin measurements relying on TDEs in the upper SMBH range.

Unified Astronomy Thesaurus concepts: Time domain astronomy (2109); Stellar mass black holes (1611); Supermassive black holes (1663); Tidal disruption (1696)

1. Introduction

Most galactic nuclei are characterized by an extremely high density of stars. These nuclear star clusters (NSCs), which are unrivaled in luminosity compared to any other type of star cluster, possess the densest known stellar densities (see Neumayer et al. 2020 for an extensive review). Their steep mass profiles, ranging from $\rho(r) \propto r^{-1}$ to r^{-3}, result in densities that are $\sim 10^{6}\,M_{\odot}\,\mathrm{pc}^{-3}$ at radial distances $R \sim 0.1$ pc. Their occupation fraction appears to vary with both galaxy mass and galaxy type, reaching $\gtrsim$80% in $\sim 10^{9}\,M_{\odot}$ early-type galaxies (Sánchez-Janssen et al. 2019), but it declines at both the lower- and higher-mass end. The study of NSCs is an important one in galaxy formation, their formation being tied to both the growth of galaxies as well as to their central supermassive black hole (SMBH).

The very high densities of NSCs, which contain a fraction $\sim$1% of their mass in stellar-mass black holes (sBHs; Bahcall & Wolf 1976), are very conducive to close encounters among their constituents. In particular, close encounters between sBHs and stars in the NSC can lead to tidal disruption events (TDEs), detectable by their high luminosities. The occurrence of these events in NSCs is especially important in that it has been shown to help calibrate the number of sBH binaries in these systems (Fragione et al. 2021).

Here we note an interesting new phenomenon. When a star in the NSC undergoes a TDE by an sBH (Perets et al. 2016), some fraction of the debris remains bound and accrete to the sBH, while the rest gets unbound. However, there is a range of locations of the sBH for which this unbound debris, while escaping from the sBH, remains bound to the SMBH, to which it hence returns, causing a second, longer flare. In this Letter, we quantify the conditions under which the sBH-unbound debris remain SMBH bound, as a function of the relevant variables of the problem, which is the sBH location, the SMBH mass, and the debris ejection angle. We compute the fallback rates for a number of representative cases, discovering a variety of resulting temporal slopes that can yield a varied range of electromagnetic transients. We finally compute the event rates per galaxy of these double-flaring events, showing that they can be as high as the standard TDE rates, depending on the SMBH mass.

Our Letter is organized as follows: Section 2 illustrates the geometry of the problem and the orbital properties of the debris. Fallback rates are presented in Section 3, together with a discussion of the electromagnetic signatures of the double-flaring event. We compute the rate in Section 4. We summarize and discuss the implications of our results in Section 5.

2. Orbit of the Debris around an SMBH–sBH System

We consider a TDE where an $m_{\star} = 1\,M_{\odot}$ and $r_{\star} = 1\,R_{\odot}$ main-sequence star is tidally disrupted at the tidal radius $r_{\mathrm{t}} = (m_{\bullet}/m_{\star})^{1/3} r_{\star}$ by an sBH with mass $m_{\bullet}$ moving on a circular orbit around an SMBH at a distance R. For simplicity, we assume that the original orbit of the star relative to the sBH is parabolic and the sBH–SMBH orbit aligns with the orbit of the disrupted star around the sBH (thus in the same orbital plane).

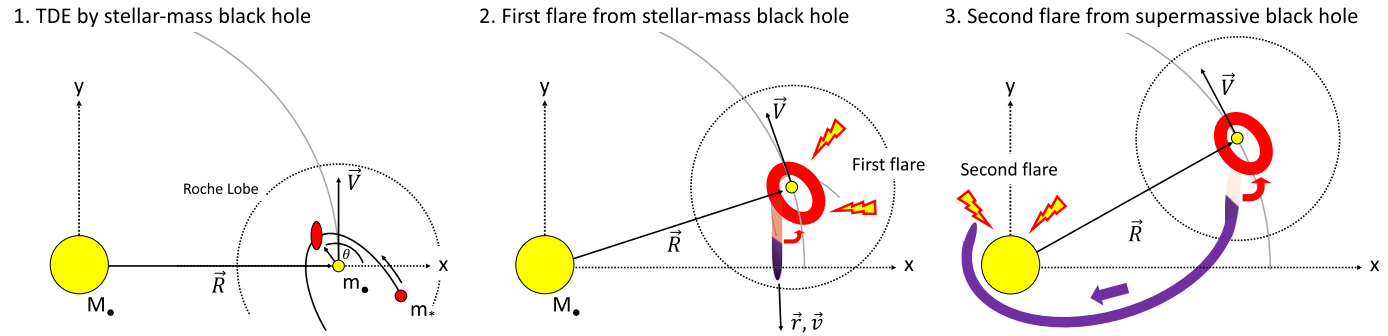

Figure 1. Schematic diagram for a double-flare event in a 2D configuration. While an sBH (small yellow circle) is orbiting around an SMBH (large yellow circle), it tidally destroys a star (red circle) (left). The angle of the incoming star's orbit at disruption relative to the line connecting the sBH and SMBH is θ. The debris bound to the sBH returns and creates the first flare (middle). The debris, originally unbound from the sBH, spills out of its RL. If the kinetic energy of the spilled debris is not sufficiently high, it remains bound to the SMBH and falls into it, creating the second flare (right). The diagram is not to scale.

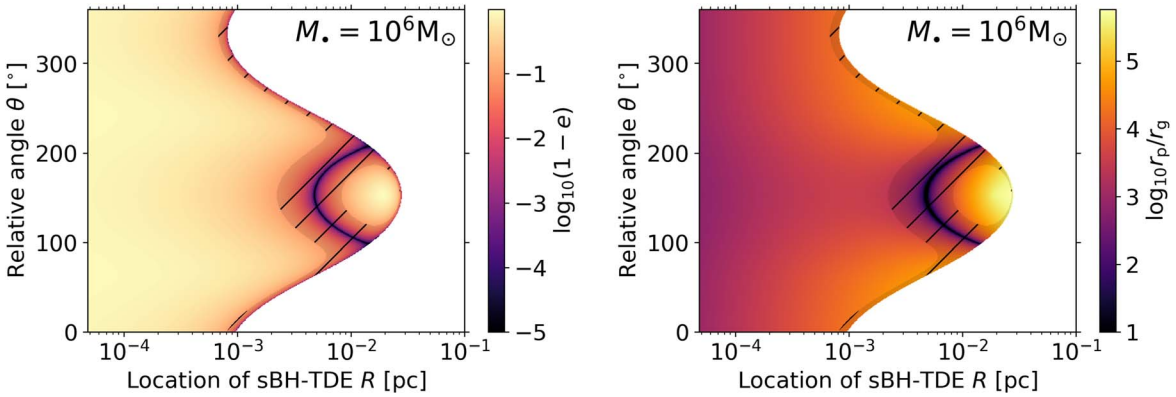

Figure 2. Eccentricity e (left) and pericenter distance r_p (right) of the "spilled" debris unbound from the sBH but bound to the $10^6\,M_\odot$ SMBH. Those quantities are measured for the debris's orbit relative to the SMBH. In both panels, the hatched regions indicate highly eccentric debris ($e > 0.9$). The region with a white background indicates debris unbound from the SMBH. The binding energy of the spilled debris relative to the SMBH is determined by its kinetic energy at the point it escapes the RL around the sBH at a given location. The debris moving in the opposite direction to the sBH ($\theta \simeq 180°$) tend to have less kinetic energy and smaller angular momentum, resulting in a more bound and more eccentric orbit around the SMBH. As the distance of the sBH TDEs from the SMBH gets smaller, the kinetic energy of the sBH is more dominant with respect to the debris's kinetic energy, leading to the spilled debris's orbit becoming more similar to that of the sBH.

2.1. The Orbit of the Debris Originally Bound to the sBH

Most of the debris originally bound to the sBH would return to the sBH, creating the first flare. However, some fraction of the originally bound debris is still energetic enough to go beyond the Roche lobe (RL) of the sBH, subsequently falling into the SMBH. As an order of magnitude estimate, the minimum energy required to reach the RL radius of the sBH $r_{\rm RL} \simeq (m_\bullet/3M_\bullet)^{1/3}R$ is $\simeq -Gm_\bullet/[2r_{\rm RL}]$. Assuming a top-hat energy distribution ($dm/d\epsilon \simeq m_\star/2\Delta\epsilon$, where ϵ is the debris's orbital energy relative to the sBH and $\Delta\epsilon = Gm_\bullet r_\star/r_t^2$), the fraction of originally bound debris mass that can escape the RL of the sBH, relative to the stellar mass, can be roughly estimated as

$$f_{>r_{\rm RL}} \simeq \frac{Gm_\bullet/[2r_{\rm RL}]}{\Delta\epsilon},$$
$$\simeq 10^{-4}\left(\frac{M_\bullet}{10^6\,M_\odot}\right)^{1/3}\left(\frac{m_\bullet}{10\,M_\odot}\right)^{1/3}\left(\frac{m_\star}{1\,M_\odot}\right)^{-2/3}$$
$$\times\left(\frac{r_\star}{1\,R_\odot}\right)\left(\frac{R}{10^{-2}\,{\rm pc}}\right)^{-1}. \quad (1)$$

This estimate suggests that the bound debris is mostly contained within the RL of the sBH, and only a small fraction may flow toward the SMBH for very massive SMBHs. Therefore, in the following we will assume that the entire originally bound debris stays within the RL of the sBH and is responsible for creating the first flare.

2.2. The Orbit of the Originally Unbound Debris

We first consider the orbit of the most energetic ejecta relative to the sBH. Within the RL of the sBH, its position and velocity in the frame of the sBH can be described by a hyperbolic orbit with $\epsilon = \Delta\epsilon$ and angular momentum such that the pericenter distance is the tidal radius r_t from the sBH. Here, we introduce the angle θ between the line connecting the sBH and the SMBH and the orientation of the star's orbit relative to the sBH (see the left panel of Figure 1).

The time $t_{\rm RL}$ it takes for the most energetic debris to reach the RL can be estimated numerically. $t_{\rm RL}$ is generally longer than the peak fallback time of the most bound debris (relative to the sBH) except for very small R and $M_\bullet$ (e.g., $R < 10^{-4}$ pc and $M_\bullet \simeq 10^5\,M_\odot$). This means it is plausible that the first TDE-like flare from the sBH can be generated, while the most unbound ejecta is rushing toward the surface of RL of the sBH (middle panel of Figure 1).

Once the unbound debris reaches the RL boundary, the subsequent orbit would be governed by the potential of the SMBH. Figure 2 shows the eccentricity e (left) and pericenter

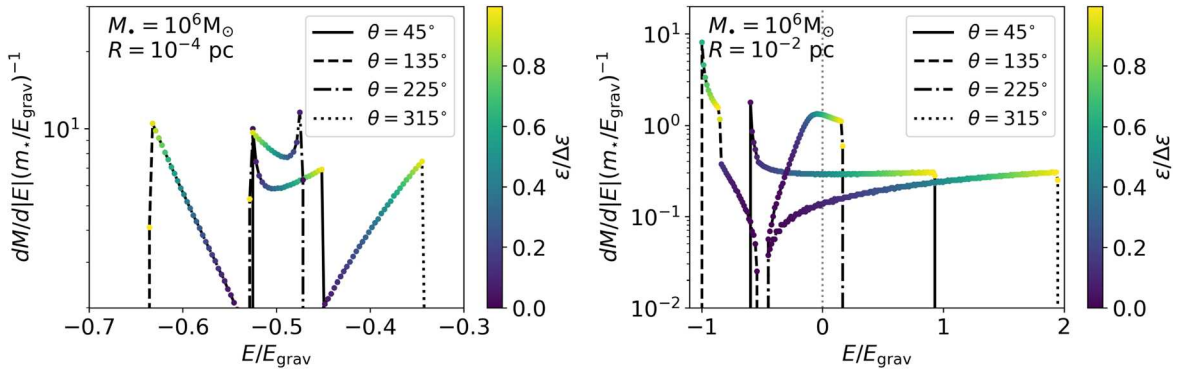

Figure 3. The energy distribution dM/dE of debris, originally unbound from the sBH, in the frame of the $10^6\,M_\odot$ SMBH. $E_{\rm grav}$ is the local gravitational potential, $G\,M_\bullet/R$. The colors show how much the debris was unbound from the sBH originally: most unbound (yellow) to least unbound (blue).

distance $r_{\rm p}$ (right) of "spilled" debris relative to the $M_\bullet = 10^6\,M_\odot$ SMBH, as a function of R and θ. The most energetic spilled debris produced in sBH TDEs at $R \lesssim 10^{-3}$–10^{-2} pc is bound to the SMBH, whereas the debris in sBH TDEs at larger distances is unbound from the SMBH (white background). To zeroth order, the critical distance $\widehat{R}$ demarcating regions for the bound and unbound debris can be estimated by comparing the potential at the location of the sBH $E_{\rm grav} = -\,GM_\bullet/R$ and the energy of the spilled debris $\Delta\epsilon$ (relative to the sBH). If $|E_{\rm grav}| \gg \Delta\epsilon$, the spilled debris does not have kinetic energy large enough to escape from the SMBH. However, if $|E_{\rm grav}| \ll \Delta\epsilon$, the spilled debris would escape. It follows that the critical distance is roughly

$$\widehat{R} \simeq \frac{GM_\bullet}{\Delta\epsilon} \simeq 0.01\ {\rm pc}\left(\frac{M_\bullet}{10^6\,M_\odot}\right) \times \left(\frac{m_\bullet}{10\,M_\odot}\right)^{-1/3}\left(\frac{m_\star}{1\,M_\odot}\right)^{-2/3}\left(\frac{r_\star}{1\,R_\odot}\right), \quad (2)$$

which suggests that $\widehat{R}$ only depends on $M_\bullet$ for given θ, $m_\bullet$, and $m_\star$. We confirm that the distributions of e and $r_{\rm p}$ shown in Figure 2 shift horizontally while maintaining their dependence on θ.

The comparison between $|E_{\rm grav}|$ and $\Delta\epsilon$ allows us to understand the distribution of e better (left panel of Figure 2). The debris produced closer to the SMBH tends to be more circular because the motion of the spilled debris is almost the same as that of the sBH given $\Delta\epsilon \ll |E_{\rm grav}|$. As shown in the right panel, highly eccentric debris that can approach very close to the SMBH is mostly generated near $\widehat{R}$, where $\Delta\epsilon \simeq |E_{\rm grav}|$.

3. Energy Distribution, Fallback Rates, and Electromagnetic Signatures

3.1. Energy Distribution

Now we extend our analysis to the entire spilled debris. Here, we assume a top-hat energy distribution ($dM/d\epsilon = m_\star/2\Delta\epsilon$) of originally unbound debris relative to the sBH (Rees 1988). The energy distribution dM/dE of the spilled debris in the frame of the $10^6\,M_\odot$ SMBH is diverse and depends on θ, R, and $M_\bullet$. Here, E represents the orbital energy relative to the SMBH. As an example, we show in Figure 3 dM/dE when an sBH TDE happens at $R = 10^{-4}$ pc (left) and 10^{-2} pc (right). At $R = 10^{-4}$ pc, $\Delta\epsilon \simeq E_{\rm grav}$ (more precisely $\Delta\epsilon = 0.44E_{\rm grav}$). Consequently, while the energy distributions are concentrated near $E = 0.5E_{\rm grav}$, corresponding to the circular orbit of the sBH, the angle dependence spreads the distributions around $0.5E_{\rm grav}$. The maximum range of $E/E_{\rm grav}$ would roughly be $-0.5E_{\rm grav} \pm \Delta\epsilon$. The eccentricity of the debris's orbit around the SMBH is 0.1–0.25.

On the other hand, at $R = 10^{-2}$ pc, $\Delta\epsilon \gg E_{\rm grav}$. As a result, as shown in the right panel of Figure 3, the energy distribution has a stronger θ dependence, and it can spread over a wide range of E. The eccentricity of the debris's orbit relative to the SMBH in this case ranges from 0.1 to 1, with a tendency of less bound debris (to the SMBH) on more eccentric orbits except for $\theta = 45°$. This suggests that while the more-energetic debris, originally the more-unbound debris from the sBH, escapes the RL of the sBH at an earlier time, it would take a longer time for the debris to reach its pericenter on a more eccentric orbit around the SMBH.

As expected from the relation between $\Delta\epsilon$ and $E_{\rm grav}$, the energy distribution is degenerate between $M_\bullet$ and R for given $m_\bullet$ and $m_\star$. In other words, the energy distribution $dM/d(E/E_{\rm grav})$ would look identical for the same $M_\bullet/R$. For example, the distribution shown in the left panel of Figure 3 is the same as that for $M_\bullet = 10^8\,M_\odot$ and $R = 10^{-2}$ pc.

3.2. Fallback Rates

We compute the fallback rate under the common "frozen-in" approximation for TDEs by SMBHs (Rees 1988), where the debris is assumed to follow ballistic orbits following impulsive destruction of the star at the pericenter. Similarly, in our case, we assume that the spilled debris outside the RL of the sBH follows a ballistic orbit in the gravitational potential of the SMBH. The fallback rate may then be estimated as

$$\dot{M}_{\rm fb} = \frac{dM}{dt} = \frac{dM}{dE}\left|\frac{dE}{dt}\right|, \quad (3)$$

where dE/dt is computed as the analytic derivative of the energy with respect to the period, assuming ballistic orbits. The fallback rate is displayed in Figure 4 for sBH TDEs at $R = 10^{-2}$ pc from the $10^6\,M_\odot$ SMBH (see the right panel of Figure 3 for dM/dE). Depending on θ (also R and $M_\bullet$), the shape of the mass-return curves varies. This is a clear difference from ordinary TDEs, where fallback curves are generally described by a rapid rise and power-law decay following a $t^{-5/3}$ power law. In some of our cases, the fallback-rate curve follows the $t^{-5/3}$ power law (e.g., $\theta = 225°$), where dM/dE becomes flat. However, even in those cases, the slopes of the rising curves and the shape at the peak are different from each other.

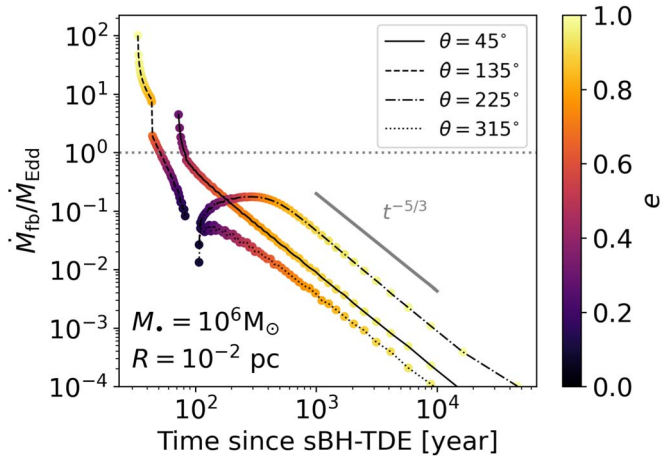

Figure 4. The returning rate of the spilled debris, originally unbound from the sBH following an sBH TDE at distance R, to the SMBH for a range of values of θ. $\dot{M}_{\rm Edd} = L_{\rm Edd}/c^2$, where $L_{\rm Edd}$ is the Eddington luminosity. The lines are color-coded based on the mass-weighted average eccentricity. Unlike ordinary TDEs, the fallback rates can have a variety of shapes, depending on θ, R, and $M_\bullet$, including the $t^{-5/3}$ power-law decay.

The peak mass-return rate can be super-Eddington, and the mass-return time is roughly of the order of the free-fall time at R. Given the scaling relation of dM/dE with $M_\bullet$ and R, the fallback time scales as $\propto M_\bullet$ and $\dot{M}/\dot{M}_{\rm Edd} \propto M_\bullet^{-2}$ for a given $M_\bullet/R$. In other words, for $M_\bullet = 10^8\,M_\odot$ and $R = 1$ pc, the overall shape of the fallback curves is the same as that shown in Figure 4, while the rate decreases by 4 orders of magnitude and the return time increases by a factor of 100. So the mass-return rates for that case become sub-Eddington, and the return times become longer than 3000 yr.

Another difference from ordinary TDEs is that the debris has a wide range of eccentricity and, therefore, pericenter. In these particular cases shown in Figure 4, except for $\theta = 45°$, the spilled debris, originally less unbound from the sBH ($\epsilon \simeq 0$), becomes more tightly bound to the SMBH, reaching the pericenter on a relatively low-e orbit at earlier times. As a result, the peak mass-return rate corresponds to the return of low-e, tightly bound debris.

3.3. Electromagnetic Signatures

Broadly speaking, the events are characterized by two flares, separated by a time delay. The first electromagnetic signature is produced by the tidal disruption of the star by the sBH. These sBH TDEs (Perets et al. 2016) have been studied via numerical simulations with sBHs in isolation as well as in binaries (Kremer et al. 2019; Lopez et al. 2019; Wang et al. 2021; Ryu et al. 2022, 2023a, 2023b, 2024a; Kremer et al. 2022). Unlike the case of TDEs around SMBHs, cooling in the debris is found to be inefficient, resulting in the formation of an optically thick remnant disk. The low mass of the sBHs results in accretion rates (taken as a proxy of the fallback rates), which are very high, possibly exceeding the Eddington luminosity by many orders of magnitude (e.g., Wang et al. 2021; Kremer et al. 2019). Under these conditions, strong wind/outflows are likely to develop (Sadowski et al. 2014) and, in combination with the high accretion–induced spin, likely to launch a jet (Krolik & Piran 2012). These conditions resemble those leading to the formation of gamma-ray bursts (GRBs), and in fact, sBHs have been proposed as possible progenitors for the subclass of ultralong GRBs (Levan et al. 2014), characterized by bright gamma-/X-ray flares of durations $\sim 10^3$–10^4 s and luminosities generally $\sim 10^{48}$–10^{49} erg s^{-1} but occasionally as low as $\sim 10^{46}$ erg s^{-1}.[5] Reprocessing of the high-energy radiation within the outflow could also give rise to optical luminosity (Kremer et al. 2019).

This first flare is followed by the second flare once the sBH-unbound debris starts to fall back onto the SMBH. This timescale can be evinced by Figure 4, here explicitly shown for the case of $M_\bullet = 10^6\,M_\odot$. It is evident that the rate at which the debris rains back is highly dependent on the angle at which the plunge begins.

Once fallback begins, the subsequent detailed evolution of the gaseous debris is largely determined by its ability to circularize in a disk. In contrast to the case of standard SMBH TDEs, where the debris are typically highly eccentric and circularization requires a significant amount of energy dissipation through a combination of effects (such as thermal viscous and magnetic shears, compression of the stream at pericenter, general relativistic apsidal precession; see, e.g., Piran et al. 2015; Chen & Shen 2018), the spilled debris is dominated by low eccentricities (see the left panel of Figure 2) for some cases, with the most bound material being the most circular one. Hence, the formation of a disk or a ring is likely to occur for the spilled debris.

Upon circularization, the subsequent evolution of a disk is set by the viscous timescale (Shakura & Sunyaev 1973). At high accretion rates, the flow is likely to be at least partly dominated by radiation pressure (Abramowicz et al. 1988), which tends to make it puffier. The viscous timescale can be written as

$$t_{\rm visc} \simeq \frac{1}{\alpha}\left(\frac{R_{\rm circ}^3}{GM_\bullet}\right)^{1/2}\left(\frac{H}{R_{\rm circ}}\right)^{-2} \simeq 1.3\ {\rm yr}\left(\frac{\alpha}{0.1}\right)^{-1}\left(\frac{R_{\rm circ}}{10^3 r_{\rm g,6}}\right)^{3/2} \times \left(\frac{M_\bullet}{10^6\,M_\odot}\right)^{-1/2}\left(\frac{H/R_{\rm circ}}{0.2}\right)^{-2}, \quad (4)$$

where α is the viscosity parameter (Shakura & Sunyaev 1973), $R_{\rm circ}$ the circularization radius, H the disk scale height, and $r_{\rm g,6}$ is the gravitational radius of a $10^6\,M_\odot$ SMBH. Note that, for an order of magnitude estimate, the above equation assumes the circularization radius to be at the pericenter of the spilled debris, but in reality there will be a spread of initial locations. As a reference, we normalized the equation using a moderate value for the disk scale height, however, bearing in mind that there are likely going to be thickness variations across different events (e.g., van Velzen et al. 2019).

Generally speaking, in the case where the circularization is efficient, if the viscous timescale is shorter than the fallback time, then the accretion rate onto the SMBH tracks the fallback rate. Conversely, if the viscous timescale is longer, then the accretion rate will be modulated by the viscous timescale. Here we find the former situation to be true for most parameters, and hence, we can assume to first approximation that the time evolution of the accretion rate $\dot{M}_{\rm acc}$ tracks that of the fallback rate. The time delay between the high-energetic flare of the

[5] Also of possible interest is the transient Swift J1644 + 57 (Levan et al. 2011), which occurred in the nucleus of a galaxy and which was interpreted both as a TDE (Bloom et al. 2011) as well as an ultralong GRB (Quataert & Kasen 2012).

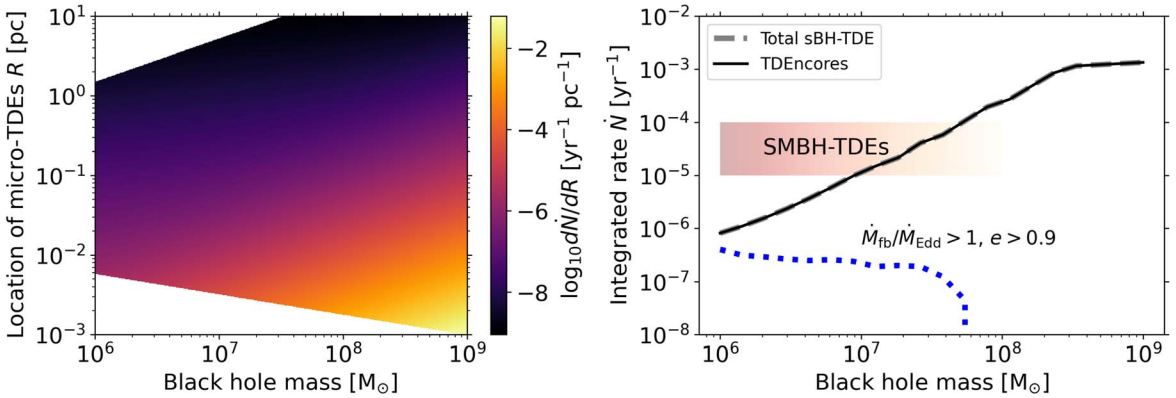

Figure 5. Differential rates of all sBH TDEs of 1 $M_\odot$ stars by 10 $M_\odot$ BHs (left) and integrated rates (right). In the right panel, the gray solid line depicts the total rate for sBH TDEs, and the black dashed line depicts the rate for sBH TDEs producing the debris that could potentially fall into the SMBH and creating flares. Their rates are almost identical because most of sBH TDEs happen close to the SMBH where the spilled debris is tightly bound to the SMBH. Note that the fallback rates of the spilled debris are super-Eddington in almost all sBH TDEs. In addition, the rate of events with the debris falling at a super-Eddington fallback rate on highly eccentric orbits ($e \gtrsim 0.9$) is depicted with the blue dotted line. The SMBH-"TDE"-like rates are indicated using the orange horizontal strip.

sBH TDE and the peak of the second flare depends on a combination of parameters, as illustrated in Figure 4 and discussed in the previous subsection. The later-arrival flares are generally dimmer than the prompt arrivals, with a decay slope following the characteristic $t^{-5/3}$ law. The peak bolometric luminosity, $L_{\rm bol} = (\eta/0.1)\dot{M}_{\rm acc}c^2$, of these later flares is generally sub-Eddington but can still reach luminosities compared with those of the standard TDEs. In the specific example of Figure 4, the peak bolometric luminosities for all the plunging angles, except for $\theta = 135°$, are in the range $L_{\rm bol} \sim (\eta/0.1)5 \times 10^{42}$–$5 \times 10^{44}$ erg s^{-1}. These luminosities, combined with the "typical" TDE time evolution and the very long delay $\gtrsim$100 yr from the sBH-TDE flare, would make these events appear as "impostors" in a galactic nucleus.

The debris spilling from an angle $\theta = 135°$, on the other hand, being in a more radial trajectory toward the SMBH, have a much shorter fallback time and can reach the SMBH on $\sim$ yr timescale following the microflare. Note that the early debris is characterized by a high eccentricity, and hence some form of dissipation, as for the standard TDEs, is required for them to circularize. A flare produced by this debris would be characterized by a rather high bolometric luminosity, approaching $\sim(\eta/0.1)10^{45}$ erg s^{-1} for the example shown in Figure 4. But what makes second flares of this kind especially stand out is their very steep time evolution, $\propto t^{-3} - t^{-4}$, in the early phase. While deviations from the classical $t^{-5/3}$ are generally expected in the optical also for standard TDEs (Lodato & Rossi 2011), such steep power laws are not generally predicted, and hence, when observed, could be indicative of a tidal disruption encore. Measurements of the time delay between the sBH TDE and the onset time of the second flare would yield information on the location of the sBH within the NSC. Since shorter delay times correlate with closer sBHs, these types of events can provide a powerful diagnostic of the sBH population in the innermost region of NSCs.

4. Rates

Let us consider a nuclear stellar cluster with an SMBH with mass $M_\bullet$ at the center. We assume that the NSC extends out to the influence radius $r_i = GM_\bullet/\sigma^2$ of the SMBH such that the enclosed mass is the same as $M_\bullet$. Here, σ is the velocity dispersion, for which we take the $M_\bullet$–σ relation by Kormendy & Ho (2013). We also assume that the NSC consists of two stellar-mass objects, $m_\star = 1\,M_\odot$ stars and $m_\bullet = 10\,M_\odot$ sBHs, both of which follow the Bahcall–Wolf profile (Bahcall & Wolf 1976) such that the total number ratio of sBHs to stars is 0.01 (e.g., Generozov et al. 2018).[6]

The differential rate $d\dot{N}/dR$ is estimated as

$$\frac{d\dot{N}}{dR} = \frac{dN_\bullet}{dR} n_\star(R)\Sigma(R)v(R), \tag{5}$$

where $dN_\bullet/dR$ is the number of sBHs at R within R and $R + dR$, $n_\star$ is the stellar number density, and v the maximum of $\sqrt{GM_\bullet/R}$ and σ. $\Sigma(R)$ is the encounter cross section, estimated as

$$\Sigma(R) = \pi r_{\rm t}^2\left(1 + \frac{GM_\bullet}{r_{\rm t}v^2}\right), \tag{6}$$

where $r_{\rm t} = (M_\bullet/m_\star)^{1/3}r_\star$ is the tidal disruption radius.

We first show the differential rate $d\dot{N}/dR$ as a function of $M_\bullet$ and R in the left panel of Figure 5. sBH-TDE rates are higher at smaller R because of larger $dN_\bullet/dR$ and $n_\star$. In addition, at $R \lesssim 5 \times 10^{-3}$ pc $(M_\bullet/10^6\,M_\odot)$, $GM_\bullet/[r_{\rm t}v^2] < 1$, and $d\dot{N}/dR \propto v \propto R^{-1/2}$, indicating a larger v near the SMBH also increases the rate. In addition, $dN_\bullet/dR$ increases with $M_\bullet$: $dN_\bullet/dR \propto M_\bullet^{0.3}$. Combining all these factors, $d\dot{N}/dR \propto M_\bullet^{1.14}$ for $R \ll 5 \times 10^{-3}$ pc $(M_\bullet/10^6\,M_\odot)$ and $d\dot{N}/dR \propto M_\bullet^{0.14}$ for $R \gg 5 \times 10^{-3}$ pc $(M_\bullet/10^6\,M_\odot)$.

We estimate the total rate as $\dot{N}(M_\bullet) = \int_{r_0}^{r_i}(d\dot{N}/dR)dR$. Here, the integration lower r_0 limit is the maximum among the following distances: (1) $10r_{\rm g}$, (2) $r_{\rm t}$, and (3) R, above which there is at least one sBH and one star. For $M_\bullet \lesssim$ a few $10^8\,M_\odot$, r_0 is set by the distance at which $N_\bullet = 1$, while it is set by $10r_{\rm g}$ for larger $M_\bullet$ (see Appendix and Figure 6 for the expressions of those distances and their values as a function of $M_\bullet$). The total rate is depicted in the right panel of Figure 5. The total rate increases from 10^{-6} yr^{-1} gal^{-1} for $M_\bullet \simeq 10^6\,M_\odot$ to $\simeq 10^{-3}$ yr^{-1} gal^{-1} for $M_\bullet \simeq 10^9\,M_\odot$. The rate for events involving super-Eddington fallback (red line) is comparable to the total rate. Among those events, the rate of events involving super-Eddington fallback of the debris on highly eccentric orbits (blue) is quite low: $\dot{N} \lesssim$ a few $10^{-7}\,M_\odot$ for $M_\bullet \lesssim 3 \times 10^7\,M_\odot$.

[6] The mass ratio of the two populations would be also time dependent. If stars are ejected at higher rates, the ratio could be even higher (Gieles et al. 2021).

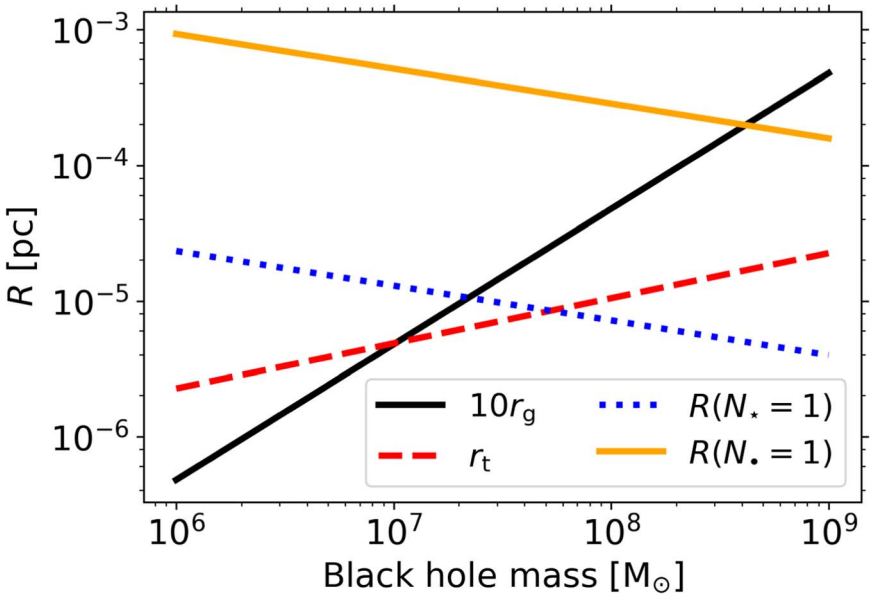

Figure 6. Several distances that determine the lower limit in the integration for the event rate: $10r_g$ (black solid), tidal radius r_t (red dashed), the minimum distance at which there is at least one star $R(N_\star = 1)$ (blue dashed), and the minimum distance at which there is at least one sBH $R(N_\bullet = 1)$ (orange solid). The maximum of those distances is used as the integration lower limit for the total rate calculation.

Note that there are a few caveats in this estimate. First, NSCs and SMBHs coexist in almost all galaxies with mass $\lesssim 10^9$–$10^{10}\,M_\odot$, corresponding to $M_\bullet \lesssim 10^8\,M_\odot$, whereas NSCs are less common toward the high galaxy mass end (Neumayer et al. 2020). Therefore, not every galaxy hosting a $\gtrsim 10^9\,M_\odot$ SMBH would create sBH TDEs as often as our rate estimate suggests. Second, stellar collisions are likely to be more frequent than sBH TDEs and could possibly be destructive (Balberg et al. 2013; Balberg & Yassur 2023; Amaro Seoane 2023; Rose et al. 2023; Ryu et al. 2024b). Such destructive collisions can have a substantial impact on the stellar distribution in the vicinity of SMBHs, where sBH TDEs are expected to be frequent. Consequently, destructive stellar collisions can significantly reduce the rate of sBH TDEs. Lastly, we count all events where the closest approach distance of the star to the sBH is smaller than r_t as sBH TDEs. However, in galactic nuclei, the relative orbits between the star and the sBH can be highly hyperbolic, potentially resulting in only a close flyby rather than the disruption of the star. Therefore, our rates should be considered maximum rates.

5. Summary and Conclusions

In this Letter, we propose that TDEs by sBHs in NSCs can potentially generate two distinctive electromagnetic flares, one from the sBH and a subsequent one from the SMBH. For the greatest majority of events, half the debris remains bound to the sBH, generating a first TDE-like flare, and the other half, originally unbound from the sBH, is still bound to the SMBH and hence spills back to it, potentially generating a second flare.

Our key findings of our analytic model for the properties of the spilled debris are the following:

1. The originally bound debris to the sBH would evolve in the same way as in sBH TDEs by sBHs in isolation, generating the first flare on the fallback timescale of $\simeq O$ (1) days. The originally unbound debris from the sBH would be spilled from its RL. For sBH TDEs at $R \lesssim 0.01$ pc $(M_\bullet/10^6\,M_\odot)$ (Equation (2)), even the most energetic "spilled" debris remains bound to the SMBH, falling into it and potentially creating the second flare on a timescale of $\gtrsim O(1)$ yr.
2. Unlike for standard TDEs, the spilled debris that remains bound to the SMBH can have a wide range of energy and angular momentum, depending on various factors including the initial angle of departure of the debris relative to the motion of the sBH (θ), SMBH mass ($M_\bullet$), and the location of sBH TDEs (R). As a consequence, the shape of the fallback-rate curves varies (see Figure 4). For instance, the peak return rates can be both super-Eddington and sub-Eddington for given $M_\bullet$ and R, depending on θ. Also, it is possible that the debris on a less circular orbit can have shorter delays and higher return rates.
3. The electromagnetic signatures are characterized by a double flare: a short, gamma-ray/X-ray bright one, possibly resembling a very long GRB, followed by a dimmer second one, with bolometric luminosity consistent with the bulk of standard TDEs. Time delays vary from a few years to hundreds of years. Second flares with very long delays generally display the characteristic $\propto t^{-5/3}$, which would make these appear as "impostors" in the standard TDE population. Early and bright arrivals, on the other hand, are characterized by much steeper decays.
4. The total rates of close encounters potentially resulting in sBH TDEs with a secondary flare range from 10^{-6}–$10^{-3}\,\mathrm{yr}^{-1}\,\mathrm{gal}^{-1}$ for $M_\bullet \simeq 10^6$–$10^9\,M_\odot$. In almost all these events, the fallback rates can be super-Eddington. However, the rate of events creating the spilled debris falling back to the SMBH at super-Eddington rates on highly eccentric orbits is $\lesssim 10^{-7}\,\mathrm{yr}^{-1}\,\mathrm{gal}^{-1}$, independent of the $M_\bullet$.

Our newly discovered astrophysical phenomenon carries a broad range of implications. When a double peak is observed, either in real time or via an archive search of positionally coincident X-ray/γ-ray transients, information on the position of the sBH can be gained. More generally, rates of the double-

flare events can help calibrate the number of sBHs in the NSC. Among others, this is important for the AGN channel of BH–BH mergers (McKernan et al. 2020) since a large fraction of BHs is expected to be captured into the AGN disk from the NSC (Fabj et al. 2020; Wang et al. 2024).

Double flares with short time delays, associated with sBHs in tight orbits, could be seen during the extreme-mass-ratio inspiral of the LISA band if a star happens to be within the innermost several r_g of the SMBH (Derdzinski et al. 2021) when an sBH spirals in.

For events in which the first sBH-TDE flare is missed, the second flare from the SMBH can appear as an "impostor" among the standard TDEs from the SMBH. Interestingly, a fraction of the observed TDEs displays slopes that deviate from the canonical expectations for TDEs (Gezari 2021; Hammerstein et al. 2023)

The implications of these impostors can be particularly significant if a "TDE"-like event is observed around a very massive SMBH. TDE rates are expected to drop to zero above $\sim 10^8\,M_\odot$ for a nonrotating SMBH but only fade at around $7\times10^8\,M_\odot$ for maximally spinning SMBHs (e.g., Kesden 2012). Hence, TDE rates have diagnostic power to measure SMBH spins and even constrain a subclass of axions (Du et al. 2022). Impostors in this range of mass can affect spin measurements.

Since this has been the very first paper (to the best of our knowledge) studying the occurrence and properties of sBH TDE/SMBH TDE coupled events, we have kept our basic setup and assumptions simple, as we explain in the following. First, we assume that the orbit of the original star is parabolic. However, in galactic nuclei, the orbit can be highly hyperbolic. If hyperbolic sBH TDEs occur, the energy distribution of the debris would shift toward higher energy. This change can affect $\widehat{R}$ and the subsequent evolution of the debris around the SMBH. Second, we consider the sBH to be in a circular orbit around the SMBH. Deviations from the circular orbit would also affect the evolution of the spilled debris because its energy and angular momentum at the RL of the sBH would differ, depending on the orbital phase of the sBH. For instance, in the case with the sBH on an eccentric orbit, the orbit of the spilled debris can be eccentric (relative to the SMBH), even in sBH TDEs that happen very close to the SMBH, as opposed to the case with a circular sBH (see the left panel of Figure 2). Third, we consider coplanar cases where the star, sBH, and SMBH orbit in the same plane for simplicity, which may be a good approximation for AGN. In gas-free environments, the star's orbit relative to the sBH is not necessarily aligned with the sBH–SMBH orbit. The additional angle required to describe a nonzero mutual inclination would introduce a more complicated angle dependence. Fourth, we assume that orbit of the debris is ballistic around one of the two BHs. To zeroth order, this approximation holds when considering the orbital evolution of the debris in a system involving a large mass contrast between the sBH and the SMBH. Lastly, we assume sBH TDEs in gas-free galaxies. However, SMBHs tend to be surrounded by a gas medium (e.g., our Galactic center; Gillessen et al. 2019). In such cases, interactions of the infalling debris with surrounding gas—particularly material falling from a long distance—can affect the orbit of the debris and also lead to debris dissolution via Kelvin–Helmholtz instability (e.g., see Bonnerot et al. 2016; Ryu et al. 2024b). To accurately understand the observables and orbital evolution of debris in various environments, detailed hydrodynamics simulations with proper gravity calculations from both BHs are required, which we leave for our follow-up projects.

Acknowledgments

The authors are grateful to the anonymous referee for constructive comments and suggestions. We thank Philip Armitage and Zoltan Haiman for helpful discussions. R.P. gratefully acknowledges support by NSF award AST-2006839. The Center for Computational Astrophysics at the Flatiron Institute is supported by the Simons Foundation.

Software: matplotlib (Hunter 2007)

Appendix
Scaling Relations

We consider a cluster with mass $M_{\rm NSC}$ consisting of objects with mass m and radius r following a power-law profile,

$$\rho(R) = \rho_i\left(\frac{R}{r_i}\right)^{-\gamma}, \tag{A1}$$

where r_i is the influence radius and ρ_i is the density at $R = r_i$. Although we consider a Bahcall–Wolf profile with $\gamma = 7/4$ in this Letter, we leave γ as a free parameter in this analysis. Taking the $M_\bullet$–σ relation from Kormendy & Ho (2013),

$$\sigma = 200\ {\rm km\ s^{-1}}\left(\frac{M_\bullet}{0.309\times10^9\,M_\odot}\right)^{1/4.38}, \tag{A2}$$

the influence radius r_i is

$$r_i = \frac{GM_\bullet}{\sigma^2} \simeq 1.5\ {\rm pc}\left(\frac{M_\bullet}{10^6\,M_\odot}\right)^{0.54}. \tag{A3}$$

It follows that ρ_i, the enclosed mass of stars $M(<R)$, and differential mass dM/dR are

$$\rho_i = \frac{(3-\gamma)M_{\rm NSC}}{4\pi r_i^3} \simeq 3.1\times10^4\,M_\odot\ {\rm pc^{-3}} \left(\frac{M_{\rm NSC}}{10^6\,M_\odot}\right)\left(\frac{M_\bullet}{10^6\,M_\odot}\right)^{-1.63}, \tag{A4}$$

$$M(<R) = \frac{4\pi\rho_i r_i^\gamma}{(3-\gamma)}R^{3-\gamma} \simeq 2000\,M_\odot \left(\frac{M_{\rm NSC}}{10^6\,M_\odot}\right)\left(\frac{M_\bullet}{10^6\,M_\odot}\right)^{-1.63+0.54\gamma}\left(\frac{R}{10^{-2}\ {\rm pc}}\right)^{3-\gamma}, \tag{A5}$$

$$\frac{dM}{dR} = 4\pi R^2\rho(R) = 2.4\times10^5\,M_\odot\ {\rm pc^{-1}} \left(\frac{M_{\rm NSC}}{10^6\,M_\odot}\right)\left(\frac{M_\bullet}{10^6\,M_\odot}\right)^{(-1.63+0.54\gamma)}\left(\frac{R}{10^{-2}\ {\rm pc}}\right)^{2-\gamma}. \tag{A6}$$

The minimum distance at which there is at least one cluster member object, or $M(<R)/m = N = 1$, is

$$R(N=1) = \left(\frac{(3-\gamma)m}{4\pi\rho_i r_i^{\gamma}}\right)^{1/(3-\gamma)} \simeq 2\times10^{-5}\,\mathrm{pc}\left(\frac{M_{\rm NSC}}{10^6\,M_\odot}\right)^{-1/(3-\gamma)} \times\left(\frac{M_\bullet}{10^6\,M_\odot}\right)^{(1.63-0.54\gamma)/(3-\gamma)}\left(\frac{m}{1\,M_\odot}\right)^{1/(3-\gamma)} \quad \text{(A7)}$$

In Figure 6, we estimate several characteristic distances whose maximum is used as the integration lower limit r_i to estimate the total rate $\dot{N}$. The characteristic distances are $10r_{\rm g}$ (black solid), $r_{\rm t}$ (red dashed), $R(N_\star = 1)$ (blue dashed), $R(N_\bullet = 1)$ (orange solid), and $\bar{R}(r_{\rm t})$ (cyan dotted). $r_i = R(N_\bullet = 1)$ for $M_\bullet \leqslant$; $4\times10^8\,M_\odot$, and $r_i = 10r_{\rm g}$ $M_\bullet \geqslant 4\times10^8\,M_\odot$. The distance at the transition determines the location of the knee in the right panel of Figure 5.

ORCID iDs

Taeho Ryu https://orcid.org/0000-0003-2012-5217
Rosalba Perna https://orcid.org/0000-0002-3635-5677
Matteo Cantiello https://orcid.org/0000-0002-8171-8596

References

Abramowicz, M. A., Czerny, B., Lasota, J. P., & Szuszkiewicz, E. 1988, ApJ, 332, 646
Amaro Seoane, P. 2023, ApJ, 947, 8
Bahcall, J. N., & Wolf, R. A. 1976, ApJ, 209, 214
Balberg, J. S., Giannios, D., Metzger, B. D., et al. 2011, Sci, 333, 203
Balberg, S., Sari, R., & Loeb, A. 2013, MNRAS., 434, L26
Balberg, S., & Yassur, G. 2023, ApJ, 952, 149
Bonnerot, C., Rossi, E. M., Lodato, G., et al. 2016, MNRAS, 458, 3324
Chen, J.-H., & Shen, R.-F. 2018, ApJ, 867, 20
Derdzinski, A., D'Orazio, D., Duffell, P., Haiman, Z., & MacFadyen, A. 2021, MNRAS, 501, 3540
Du, P., Egaña-Ugrinovic, D., Essig, R., Fragione, G., & Perna, R. 2022, NatCo, 13, 4626
Fabj, G., Nasim, S. S., Caban, F., et al. 2020, MNRAS, 499, 2608
Fragione, G., Perna, R., & Loeb, A. 2021, MNRAS, 500, 4307
Generozov, A., Stone, N. C., Metzger, B. D., & Ostriker, J. P. 2018, MNRAS, 478, 4030
Gezari, S. 2021, ARA&A, 59, 21
Gieles, M., Erkal, D., Antonini, F., Balbinot, E., & Peñarrubia, J. 2021, NatAs, 5, 957
Gillessen, S., Plewa, P. M., Widmann, F., et al. 2019, ApJ, 871, 126
Hammerstein, E., van Velzen, S., Gezari, S., et al. 2023, ApJ, 942, 9
Hunter, J. D. 2007, CSE, 9, 90
Kesden, M. 2012, prd, 85, 024037
Kormendy, J., & Ho, L. C. 2013, ARA&A, 51, 511
Kremer, K., Lombardi, J. C., Lu, W., Piro, A. L., & Rasio, F. A. 2022, ApJ, 933, 203
Kremer, K., Lu, W., Rodriguez, C. L., Lachat, M., & Rasio, F. A. 2019, ApJ, 881, 75
Krolik, J. H., & Piran, T. 2012, ApJ, 749, 92
Levan, A. J., Tanvir, N. R., Cenko, S. B., et al. 2011, Sci, 333, 199
Levan, A. J., Tanvir, N. R., Starling, R. L. C., et al. 2014, ApJ, 781, 13
Lodato, G., & Rossi, E. M. 2011, MNRAS, 410, 359
Lopez, M. J., Batta, A., Ramirez-Ruiz, E., Martinez, I., & Samsing, J. 2019, ApJ, 877, 56
McKernan, B., Ford, K. E. S., & O'Shaughnessy, R. 2020, MNRAS, 498, 4088
Neumayer, N., Seth, A., & Böker, T. 2020, A&ARv, 28, 4
Perets, H. B., Li, Z., Lombardi, J. C. J., & Milcarek, S. R. J. 2016, ApJ, 823, 113
Piran, T., Svirski, G., Krolik, J., Cheng, R. M., & Shiokawa, H. 2015, ApJ, 806, 164
Quataert, E., & Kasen, D. 2012, MNRAS, 419, L1
Rees, M. J. 1988, Nat., 333, 523
Rose, S. C., Naoz, S., Sari, R., & Linial, I. 2023, ApJ, 955, 30
Ryu, T., de Mink, S. E., Farmer, R., et al. 2024a, MNRAS, 527, 2734
Ryu, T., Perna, R., Pakmor, R., et al. 2023a, MNRAS, 519, 5787
Ryu, T., Perna, R., & Wang, Y.-H. 2022, MNRAS, 516, 2204
Ryu, T., Amaro Seoane, P., Taylor, A. M., & Ohlmann, S. T. 2024b, MNRAS, 528, 6193
Ryu, T., Valli, R., Pakmor, R., et al. 2023b, MNRAS, 525, 5752
Sadowski, A., Narayan, R., McKinney, J. C., & Tchekhovskoy, A. 2014, MNRAS, 439, 503
Sánchez-Janssen, R., Côté, P., Ferrarese, L., et al. 2019, ApJ, 878, 18
Shakura, N. I., & Sunyaev, R. A. 1973, A&A, 24, 337
van Velzen, S., Stone, N. C., Metzger, B. D., et al. 2019, ApJ, 878, 82
Wang, Y., Zhu, Z., & Lin, D. N. C. 2024, MNRAS, 528, 4958
Wang, Y.-H., Perna, R., & Armitage, P. J. 2021, MNRAS, 503, 6005